Lifetime response of a liquefiable soil foundation-embankment system subjected to sequences of mainshocks and aftershocks

Christina Khalil, Fernando Lopez-caballero

Lifetime response of a liquefiable soil foundation-embankment system subjected to sequences of mainshocks and aftershocks

C. Khalil[a,b,*], F. Lopez-Caballero[a]

[a]*Laboratoire de Mécanique Paris-Saclay (LMPS) CNRS UMR-9026, Université Paris-Saclay, CentraleSupélec, École Normale Supérieure, France*
[b]*Current institution: ESITC Paris, 79 Avenue Aristide Briand, 94110 Arcueil, France*

Abstract

During their typical design working life, structures are subjected to multiple sequential earthquakes that are divided into clusters of mainshocks and aftershocks. In consequence, the induced seismic damage accumulates due to these several events in each cluster. On the other hand, the Performance Based Earthquake Engineering (PBEE) methodology presents limitations in accounting for the damage issued from multiple events and the fragility curves represent the failure probability only in one event of a given intensity.

For this purpose, this work studies the response of a given structure subjected to sequences of mainshocks - aftershocks during its lifetime. The used time histories (mainshocks) were stochastically generated from a synthetic ground motion model, whereas the aftershocks were generated from the Branching Aftershock Sequence (BASS) model. The cumulative damage measure of the

*Corresponding author
Email addresses:
khalil@esitc-paris.fr,christina.khalil@centralesupelec.fr (C. Khalil),
fernando.lopez-caballero@centralesupelec.fr (F. Lopez-Caballero)

embankment is calculated after the tested sequences. More importantly, its lifetime distribution is estimated and compared with previous results. Finally, to be compatible with the PBEE methodology, the fragility evolution of the embankment over its lifetime was calculated as to emphasize its evolution with the loading history in the soil.

Keywords: clusters, cumulative damage, lifetime distribution, fragility evolution

1. Introduction

In earthquake-prone regions, structures are exposed to seismic sequences that are composed of mainshocks, aftershocks and foreshocks. Aftershock events are usually triggered by the mainshocks due to the change in the static and dynamic stresses during the earthquake process [46]. It was shown that the aftershocks exacerbate the damage generated from the triggering mainshock and may be the reason of collapse even though they have a smaller magnitude than the triggering mainshock [69, 72, 47, 67, 57, among others]. Otherwise, the structures are designed to have a useful serviceable lifetime. But when they are subjected to multiple events over their lifetime, the induced potential damage can be interpreted as the accumulation of the damages due to all the occurred earthquake shocks [52, 20, 32].

In practice, from the Performance Based Earthquake Engineering (PBEE) methodology, structures are designed to resist the first damaging earthquake scenario. Hence, the classical fragility curves represent the failure probability of one event of a given intensity only. This means that this framework neglects the cumulative damage and the evolution of the material proper-

ties resulted from multiple events [19]. In addition, the commonly used Probabilistic Seismic Hazard Analysis (PSHA) to select the corresponding ground motions, is intended to evaluate the hazards from discrete independent events. Thus, empirical scaling laws (i.e. Gutenberg-Richter, modified Omori's law, Bath's law) have been proposed to generate the aftershocks occurrence [55]. These laws are based on parameters that depend on the statistical properties of particular seismic sequences [55, 46, 61].

Previous works on buildings subjected to mainshock-aftershock events have been conducted [30, 13, 48, 46, 12, 72, 47, 31, 11, 20, 57, 40, 21, 54, among others]. In this context, researchers, have been recently interested in conducting methodologies to assess the fragility exposure of structures subjected to mainshock-aftershock events [41, 19, 9, 66, 73, among others]. Therefore, evaluating the seismic performance of structures subjected to sequential seismic events, specially when dealing with the aftershock occurrence, requires explicit consideration of the uncertainty in the state of the structure [57]. For example, the known *Incremental Dynamic Analysis (IDA)* that assesses multiple realizations to capture record-to-record response variability requires the scaling of the used seismic inputs [58, 65, 20, among others]. Then, failure is identified once the structure exceeds a threshold limit. However, in liquefaction related problems, several aspects are important to take into account. For example, the multi-physical aspects of the soil, its history of loading and its correlation with several intensity measures, are all important aspects that makes the IDA approach unrepresentative of the overall response of the geo-structure [59, 6, 36, 26].

Otherwise, several analysis exist in order to calculate or estimate the life cycle of the structure [69, 52, 48, 20, 45, 51, 32, among others]. The *Survival Analysis* has been a used approach in geotechnical engineering to identify the relative risks of various earthquake [39, 32, 26]. It is defined as the time length of the structure until the occurrence of an event of interest (i.e. equipment failure, damage, complex system) [15, 39, 7, 10, 32, 26]. It accounts for a set of statistical methods to analyze data that has the occurrence time of an event as the outcome. It calculates the probability of survival of concerned test data and estimates its Mean Time to Failure (MTTF).

In the work of Khalil and Lopez-Caballero [26], the lifetime distribution of an embankment subjected to mainshock sequences was estimated . These later were extracted from several subsets compatible with the seismic hazard of a site of concern.The site seismicity as well as the occurrence rate of mainshocks were extracted from the work of Aristizábal et al. [2]. Each subset was also in accordance with the event rate of the mainshocks and the generated time histories were permuted many times in order to take into account the randomness of the events. As a continuity of the work of Khalil and Lopez-Caballero [26] and for the same geometry and numerical model, this study will try to answer the following significant questions:

a) Is the cumulative damage of the embankment influenced by the sequence type (i.e. mainshocks sequences or mainshock-aftershock sequences) ? (Section 6)

b) Does the aftershock occurrence affects the lifetime distribution of the

embankment, as well as its MTTF ? (Section 7)

c) How do the fragility curves evolve after multiple loading histories ? Does this evolution depend on the type of the applied load ? (Section 8)

In order to answer these questions, it should be mentioned that the methodology and the PSHA of the site of concern are similar to the ones presented in the work of Khalil and Lopez-Caballero [26]. A large number of time histories is generated using stochastic simulations from the synthetic ground motion model of Rezaeian and Der Kiureghian [44]. The model used to generate the aftershocks is based on the probabilistic version of the Branching Aftershock Sequences (BASS) model and is inspired by Turcotte et al. [63] and Hu et al. [16]. Also in this paper, an interpretation of the potential failure of the embankment is developed in order to understand what happens globally in the embankment, and locally in the soil.

2. Geometry and Numerical Model

2.1. Geometry

The model's geometry is a levee of 9 m height composed of dry dense sand. The foundation is formed of 4 m loose to medium sand (LMS) on the top of a 6 m dense sand. The bedrock is located under the dense sand. The water table starts 1 m below the surface to keep the embankment dry. The inclination of the levee is a slope of 1:3 (vertical: horizontal). The geometry in this work is inspired by Rapti et al. [43], Lopez-Caballero and Khalil [33], and is detailed in Figure 1.

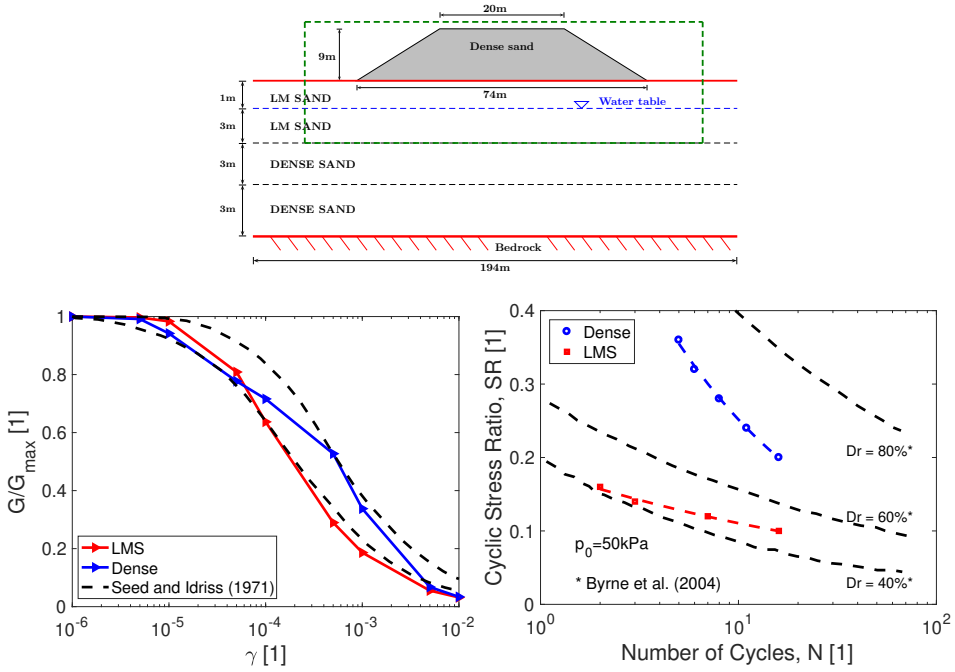

Figure 1: Geometry and behavior of the soil [33]

2.2. Soil Constitutive Model

As for the constitutive model, the *Ecole Centrale Paris (ECP)* elastoplastic multi-mechanism model (also known as *Hujeux* model) is the one chosen for this study and is written in terms of effective stress. The non-linearity of this model is represented by four coupled elementary plastic mechanism: three plane-strain deviatoric plastic strain mechanism in three orthogonal planes (k - planes) and an isotropic plane to take into account normal forces. The model follows a Coulomb type failure criterion, contemplate the existence of dilatancy/contractancy phenomena, and use the critical state concept. The cyclic behavior is taken into account by a kinematical hardening that is based on the state variables at the last load reversal. The model is written in the concept of the incremental plasticity which divides the total

strain into an elastic and a plastic part. Refer to Aubry et al. [4], Hujeux [18] and Lopez-Caballero and Modaressi-Farahmand-Razavi [34], among others, for further details about the ECP model. For the sake of brevity, only some model definitions will be developed in the following. Considering the well-known sign convention in soil mechanics which sets the positive sign to the compression forces, the yield surface of this numerical model is written in the k plane as follows:

$$f_k(\sigma, \varepsilon_v^p, r_k) \quad = \quad q_k - \sin\phi'_{pp} \cdot p'_k \cdot F_k \cdot r_k \ , \tag{1}$$

where p'_k and q_k are the effective mean and deviatoric values of the stress tensors and ϕ'_{pp} is the friction angle at the critical state. The parameters that control the behavior of the soil are F_k, which controls the isotropic hardening associated with the plastic volumetric strain and r_k, which controls the isotropic hardening generated by the plastic shearing. These two parameters represent progressive friction mobilization in the soil. At perfect plasticity, the product $F_k \cdot r_k$ reaches unity, and the Mohr-Coulomb criterion will be satisfied. Therefore, in order to measure the "distance to reach the critical state", the variable r_{apt} is calculated based on the adopted elasto-plastic numerical model and an apparent friction angle ϕ'_{apt} is defined by:

$$\sin\phi'_{apt} \quad = \quad \frac{q_k}{p'_k \cdot F_k} \tag{2}$$

$$r_{apt} \quad = \quad \frac{\sin\phi'_{apt}}{\sin\phi'_{pp}} \tag{3}$$

2.3. Finite Element Model

The computations were conducted using the coupled FE modelling code GEFDyn [3], using a dynamic approach derived from the $\underline{u} - p_w$ (i.e. $\underline{u}$ being

the displacement tensor and p_w being the pore water pressure) version of the Biot's generalized consolidation theory [74]. The FE model is composed of quadrilateral isoparametric elements (3.5 m $\times$ 1 m) with eight nodes for both solid displacements and fluid pressures. An implicit Newmark numerical integration scheme with $\gamma = 0.625$ and $\beta = 0.375$ was assumed in the dynamic analysis [29]. The FE analysis is performed in three consecutive steps: i) a computation of the initial in-situ stress state due to gravity loads; ii) a sequential level-by-level construction of the embankment and iii) a sequential seismic loading analysis in the time domain. For the computation of the sequential seismic loading, for the first motion precisely, its final effective stresses, pore-water pressures and model history variables are stored to be used as initial state for the computation of the second ground motion. The storage of the history variable of the *ith* computation will be used as initial state of the *ith+1* computation. More details regarding the calculation procedures are developed in each section.

2.4. Boundary Conditions

In the analysis, equivalent boundaries have been imposed on the nodes of lateral boundaries (i.e., the normal stress on these boundaries remains constant and the displacements of nodes at the same depth in two opposite lateral boundaries are the same in all directions). They are the response of a modeled infinite halfspace. Hence, only vertically incident shear waves are introduced into the domain. The model is wide enough (194 m) to ensure that the effect of the boundaries on the response of the model can be neglected and also to satisfy the free field condition at the lateral boundaries. For the half-space bedrock's boundary condition, paraxial elements simulating

deformable unbounded elastic bedrock have been used [38]. The incident waves, defined at the outcropping bedrock are introduced into the base of the model after deconvolution.

3. Assumptions for this study

For the following study, some assumptions are taken:

- The effect of external uncontrolled conditions (i.e. weather, rain, wind) is not considered.
- The material aging is not taken into account since it is connected to its resistance, origin and age.
- The numerical computations start after the construction phase so when the embankment is in its original state. This means that the embankment does not have a history of earthquake loading.
- The embankment is not subjected to any repairs during its lifetime.
- The constitutive model does not take into account the secondary consolidation or compression after each seismic loading.
- The cluster earthquakes consist of mainshocks and aftershocks only. The effect of foreshocks is not considered in this study.
- The stochastic ground motion model to generate the mainshocks and aftershock databases is based on the model proposed by Rezaeian and Der Kiureghian [44]. For the sake of simplicity, the same database was used to generate both types of motions.

- Only shear body waves have been used in this work. Nevertheless, any other hypothesis about the complexity of the incident wave field can be applied in the scope of this proposed methodology (e.g. [68, 62, 1, 22, among others]).

4. Model to generate Aftershocks

It is known that an earthquake event does not consist of only mainshocks, but also the occurrence of aftershocks and foreshocks. A cluster earthquake is in general composed of one mainshock with its corresponding aftershocks. The Epidemic Type Aftershock Sequence (ETAS) model has been widely used to model the statistics of seismicity [63, 16, 61, among others]. An essential feature of the ETAS model is the magnitude dependent branching (parent-daughter) ratio. In this context, Turcotte et al. [63] introduced Branching Aftershock Sequence (BASS) model as the self-similar limit of the ETAS model. Both approaches are based on empirical laws describing the distribution of earthquakes in magnitude, time and space. Four scaling relations are required in order to generate and identify the aftershocks distribution: 1) the Gutenberg-Richter (GR) frequency-magnitude scaling, 2) the Bath's law (or the modified version) for maximum-magnitude scaling, 3) Omori's law for power-law seismicity rate decay and 4) a spatial form of Omori's law. Both approaches utilize the concept of primary, second-order and higher-order aftershocks. The primary difference between the ETAS and the BASS model is in their use of the Bath's law to estimate the a-value of the GR relation; the BASS model uses the modified form of Bath's law instead of the productivity relation used in the ETAS model [63]. In addition,

the branching statistics in the BASS model are identical to the self-similar Tokunaga statistics of drainage networks [63, 70].

The following section will develop the theoretical model used to generate the corresponding aftershocks of the tested mainshocks in the work of Khalil and Lopez-Caballero [26]. It should be recalled that the used PSHA (which is based on the disaggregation of hazards) is extracted from the work of Aristizábal et al. [2] and the mainshocks were generated from the stochastic ground motion model of Rezaeian and Der Kiureghian [44]. As for the aftershocks generation (M_w, R), it is based on the BASS model to compute the distribution in magnitude and time of the aftershochs and is inspired by Turcotte et al. [63] and Hu et al. [16]. As for the location of the aftershocks, and due to the point source of the seismic propagation (i.e. no directivity effects), an Aftershock PSHA (or APSHA) is used [20]. It should be mentioned that only primary order of aftershocks is considered in this study. The theoretical equations will be developed first, and at the end of that, a summary of the used scaling relations for this study and their parameters will be presented.

4.1. Distribution of the magnitude-frequency

Similar to any seismic hazard model, the frequency-magnitude distribution of each sequence aftershock should satisfy the Gutenberg-Richter (GR) relation (Equation 4):

$$\log_{10}[N_d(\geqslant m_d)] \quad = \quad a_d - b_d m_d \ , \tag{4}$$

where m_d is the magnitude of the aftershocks, $N_d(\geqslant m_d)$ is the number of the aftershocks with magnitude greater than or equal to m_d. Parameters a_d

and b_d are constants (or known as *a-value*, *b-value* of the GR distribution). It should be noted that in practice, the magnitude of the largest aftershock Δm^* should be less than that of the triggering mainshock m_p. So

$$N_d(\geqslant (m_p - \Delta m^*)) \quad = \quad 1 \; . \tag{5}$$

It must be emphasized that this Δm^* is not the magnitude difference between the mainshock and the largest aftershock [63, 14, 70, 16, among others]. Now considering both Equations 5 and 4, The GR relation for aftershocks will be:

$$\log_{10}[N_d(\geqslant m_d)] \quad = \quad b_d(m_p - \Delta m^* - m_d) \; , \tag{6}$$

In order to terminate the sequence of aftershocks, it is necessary to specify a minimum magnitude of the aftershocks m_{min}. The total number of aftershocks N_{dT} based on Equation 6 is:

$$N_{dT} \quad = \quad N(\geqslant m_{min}) = 10^{b_d(m_p - \Delta m^* - m_{min})} \; . \tag{7}$$

Hence, the cumulative distribution function P_{Cm} for the magnitude of the aftershocks, is deduced from Equations 6 and 7. It is a random value between 0 and 1 and is given by:

$$P_{Cm} \quad = \quad \frac{N_d(\geqslant m_d)}{N_{dT}} = 10^{-b_d(m_d - m_{min})} \; . \tag{8}$$

In this study, the empirical parameters to calculate the aftershocks magnitude are $m_{min} = 4.5$, $b_d = 1$ and $\Delta m^* = 1.3$.

4.2. Distribution of the occurrence time

Knowing the magnitude of each occurring aftershock in the sequence from Equation 8, the time delay t_d until the occurrence of each aftershock after the

triggering mainshock should be known. It should be mentioned that t_d will allow to know the sequential position of each occurring aftershock. Following the generalized form of Omori's law, the rate of aftershock occurrence $R(t_d)$ would be:

$$R(t_d) \quad = \quad \frac{dN_d}{dt} = \frac{1}{\tau(1+\frac{t_d}{c})^p} \; , \tag{9}$$

where τ, c and p are given parameters. $N_d(\geqslant t_d)$ is the number of aftershocks that occurred after a time t_d:

$$N_d(\geqslant t_d) \quad = \quad \int_{t_d}^{\infty} \frac{dN_d}{dt}\, dt' = \frac{c}{\tau(p-1)(1+\frac{t_d}{c})^{p-1}} \; . \tag{10}$$

Setting $t_d = 0$ in Equation 10, the total number of aftershocks will be obtained. Hence, the cumulative distribution function P_{Ct} for the occurrence time of the aftershocks will be:

$$P_{CT} \quad = \quad \frac{N_d(\geqslant t_d)}{N_{dT}} \quad = \frac{1}{(1+\frac{t_d}{c})^{p-1}} \; , \tag{11}$$

P_{Ct} is a random value between 0 and 1 and the time of occurrence of the aftershock is deduced from Equation 11. The parameters used in this paper to calculate t_d are $\tau = 0.001$ and $p = 1.25$.

4.3. Location of the aftershocks

Concerning the seismogenic zone of the aftershock, it is assumed that each mainshock has its corresponding aftershocks located within an area around its epicenter [64, 20]. The size of this area depends on the magnitude of the triggering aftershocks as follows:

$$S_A \quad = \quad 10^{m_d - m_{min}} \; . \tag{12}$$

Within this area, considered a square, the aftershocks occur on a smaller lattice. Table 1 summarizes the parameters values of the scaling relations used for this study. Having the magnitude, distance and the time delay until the occurrence of every daughter earthquake, the generation of aftershocks time histories is feasible.

Scaling relations	**Parameters values**	**References**
GR-Bath Parameters:		
$N_{dT} = N(\geqslant m_{min}) = 10^{b_d(m_p - \Delta m^* - m_{min})}$	$b_d = 1$	Turcotte et al. [63]
$m_d = -(1/b_d) \cdot \log(P_{Cm}) + m_{min}$	$\Delta m^* = 1.3$	and Hu et al. [16]
Temporal Omori:		Turcotte et al. [63]
$t_d = \tau \cdot (P_{Ct}^{-1/(p-1)} - 1)$	$p = 1.25 \quad \tau = 0.001$	and Hu et al. [16]
Space APSHA:		
$S_A = 10^{m_d - m_{min}}$	$m_{min} = 4.5$	Iervolino et al. [20]

Table 1: The scaling relations of the magnitude, time and space distribution of the used model to generate the aftershocks

4.4. Description of the generated aftershocks

In the following, it will be described the intensity measure (IM) of the generated aftershocks. The median response spectra (structural damping ξ = 5%) of the generated mainshocks and aftershocks are shown in Figure 2a. It is clear that the spectral acceleration of the mainshocks is slighly higher than that of the aftershocks [63, 16]. Figure 2b shows a window of a sequence example. From this figure, three ideas can be validated: i) the aftershocks, if they exist, occur between two mainshocks, ii) the magnitude

of the aftershocks is less than that of the principal mainshock and iii) the mainshock of larger magnitude will generate more aftershocks comparing to the one with a small magnitude (Equation 8).

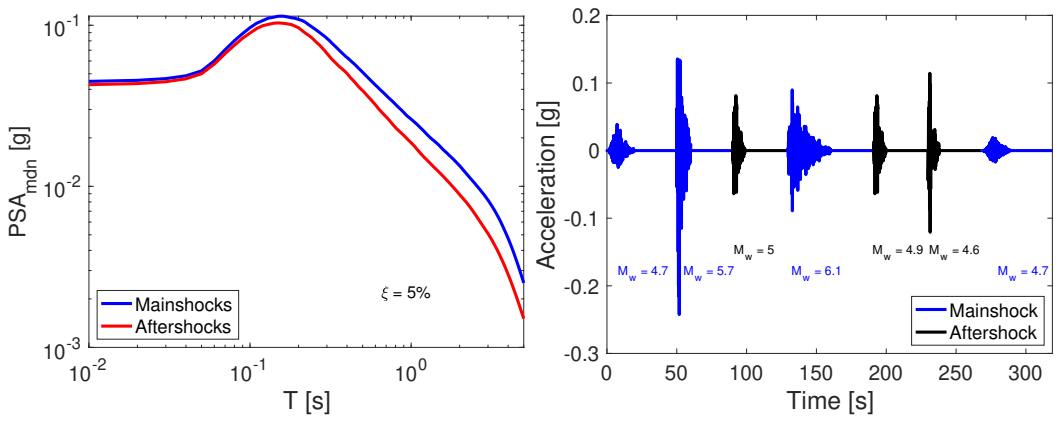

(a) (b)

Figure 2: a) The obtained median response spectra of both the generated mainshocks and aftershocks and b) a section of a sequence

Another illustration of the mainshock-aftershock parameters is shown in Figure 3. This figure considers three mainshocks (in dashed circles) with their corresponding aftershocks. Each cluster earthquake is drawn in a different shape (circle, square and diamond). Figure 3a shows a scatter plot of the outcrop acceleration $a_{max,out}$, the equivalent predominant frequency $1/T_{va}$ and the magnitude M_w. Based on Kawase [25], there exists a proportional relation between the peak ground velocity PGV, $a_{max,out}$ and $1/T_{va}$ and is represented as dashed lines. In addition to these parameters, Figure 3b shows also the variation of the source-to-site distance R. Thus, it can be seen that the corresponding aftershocks have close values of $a_{max,out}$ and $1/T_{va}$ but are in general less than those of the mainshock. In addition, the magnitude of the

mainshock is higher than that of the aftershocks, whereas the source-to-site distance of the aftershocks is close to that of the mainshocks.

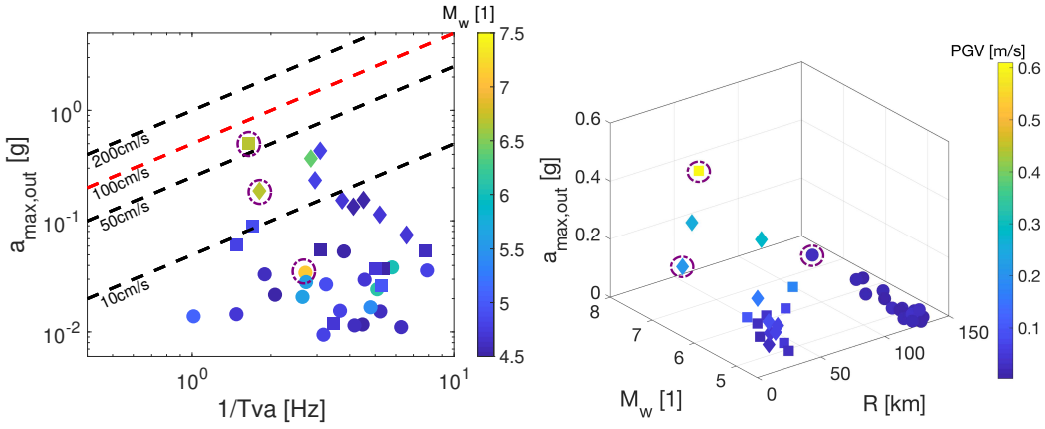

(a) (b)

Figure 3: Scatter plots of some ground motion parameters of mainshocks and aftershocks with respect to a) M_w and b) M_w and R

In order to take into account all the generated Mainshocks (MS) and the Aftershocks (AFS), Figure 4 shows a matrix form of a logarithmic comparison of some ground motion parameters. The comparison is conducted in terms of the density functions located in the diagonal of the matrix, the scatterplots and the histograms that are both located to the bottom left of the diagonal and finally, the boxplots that are located to the right.

For the density distribution function of the chosen parameters, it can be seen that the distributions of MS and AFS overlap for almost all the tested parameters, except a small change in the effective duration (D_{595}). For the median value of each database, it can be seen from the boxplots, that it is almost close for the two ground motions. Concerning the scaterplots and the histograms, they are useful to have an idea about the precise values

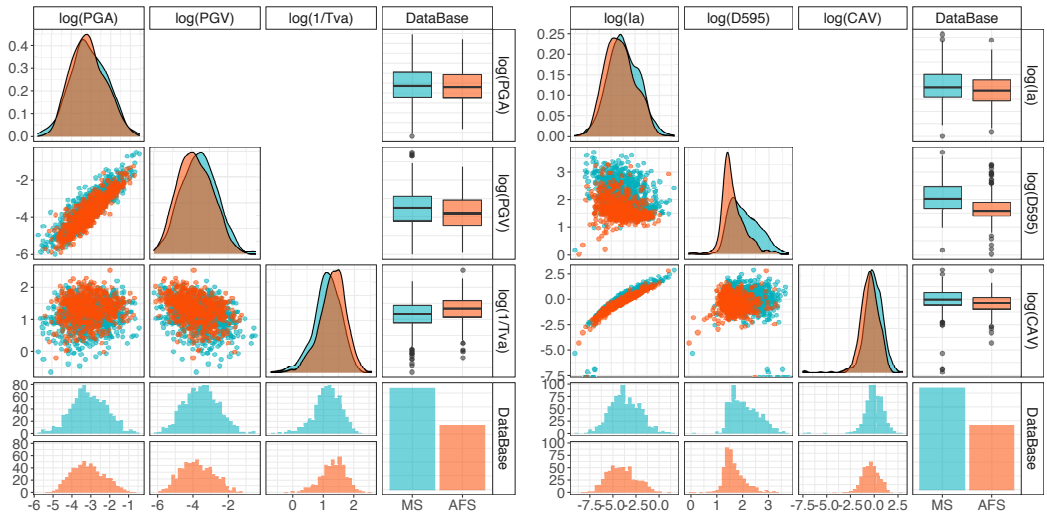

(a) (b)

Figure 4: The logarithmic distribution of some ground motion parameters of the Mainshocks (MS) and the Aftershocks (AFS)

or the relation between each parameter. After the aftershock generation, it will be analyzed in the next section the possible damage measures of the embankment and their link to the soil mechanical behavior. For this purpose, an example ground motion will be analyzed.

5. Potential embankment failure and soil behavior

The assessment of seismic structural vulnerability has broadened the objectives of seismic design so that not only the safety against collapse is the required criteria but also the long term resistance of the structures. A great effort has been made to improve the current earthquake-resistant design methods in order not only to avoid collapse under a destructive earthquake, but also to limit the damage under moderate earthquakes [8]. In engineering

practices, a stability analysis is required in order to define a safety index above which the structure will reach failure. This later is commonly known by the factor of safety FS. It is typically defined as the ratio of the available shear strength to the shear stress required to maintain the equilibrium along the prescribed failure surface [17, 28, 37, among others]. The basic idea for stability analysis, specially for soils, is to calculate at each point in a domain of interest, the so-called local factor of safety LFS. It is defined as the ratio of the potential mean stress to the current mean stress under the Mohr-Coulomb failure criterion [37].

Furthermore, the damage indices used to measure the potential structural failure are either defined for each structural element (local) or related to the entire structure (global) [8]. In this study, the potential failure and damage state of the embankment are going to be examined. For the sake of brevity only, one example ground motion will be analyzed in details. The acceleration time history at the bedrock for this example is shown in Figure 5a. Typically, the global structural failure for any similar geo-structure (the embankment) is to calculate the relative crest settlement $u_{z,rel}$. Thus, Figure 5b shows the evolution of $u_{z,rel}$ and the excess pore water pressure ratio r_u (i.e. $= \Delta p_w / p'_0$) for a point placed under the center of the embankment, at 3 m depth. It should be mentioned that 30 seconds of zero values were added at the end of the ground motion in order to ensure the recovery time (i.e. the Δp_w dissipation) of the soil foundation. It is clear from Figure 5b that at the beginning of the motion, $u_{z,rel}$ and r_u were zero. When the strong phase of the motion starts the relative crest settlement decreases rapidly, in parallel, the excess pore water pressure is generated which results in peak values for

r_u. After the strong phase, the crest settlement is constant and the excess pore water pressure dissipates. Thus, from Figure 5, it was shown that there is a link between the evolution of the vertical displacement with the excess pore water pressure dissipation.

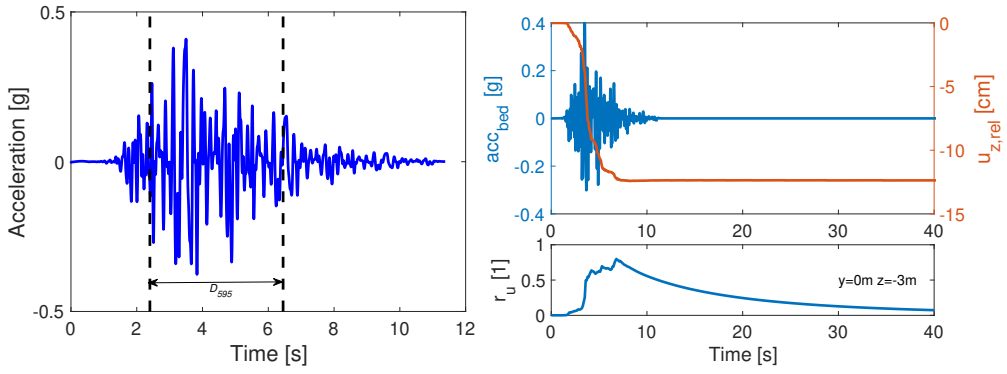

(a) (b)

Figure 5: The example a) ground motion of this section and b) the evolution in time the relative crest settlement $u_{z,rel}$ and the excess pore water pressure ratio r_u (i.e. $= \Delta p_w / p'_0$)

In order to have a complete idea about the response of the soil foundation-embankment system, the distribution of the vertical co-seismic displacement at the end of the earthquake loading was calculated. Since the liquefaction induces settlement (as shown in Figure 5), the results of Figure 6 show that the damage of the soil foundation is located under the embankment towards the free field [28, 27, 49, 42, among others].

As for the potential failure of the embankment from a local damage index, a local safety factor LFS could be estimated by calculating the residual strength. The LFS discussed in this paper is the one proposed by Lopez-Caballero and Modaressi-Farahmand-Razavi [35] and Rapti et al. [43] and derived from the yield surface of the model (Equation 1). The parameter r_{apt}

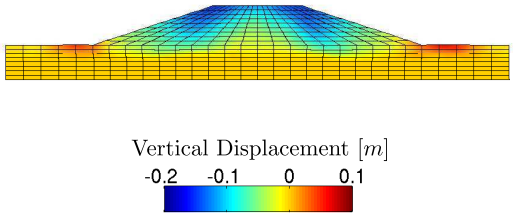

Figure 6: Enlarged view of typical vertical co-seismic displacement contours at the end of the shaking

(Equation 2) provides, for any soil state, a direct measure of the "distance to reach the critical state".

It varies between 0 and 1 where perfect plasticity is reached and could be defined as the inverse of a local safety factor ($r_{apt} = 1/LFS$). Thus, the potential mean stress is evaluated from the friction angle at the critical state ϕ'_{pp} and the current mean stress from the apparent friction angle ϕ'_{apt}. A threshold value of the damage measure is taken as 0.75 (i.e. corresponds to $LFS \approx 1.33$). This value was chosen based on sensitivity analysis performed in previous works on the same geometry [35, 43]. The domain of interest in which the local damage r_{apt} is calculated is composed of the liquefied layer with the embankment (i.e. the green window in Figure 1). It was chosen vertically due to the depth of the liquefiable layer (4 m) and laterally because of the possible zones where the failure pattern could occur.

In order to explain the function of this local damage measure, Figure 7 considers the threshold value of r_{apt} (i.e. 0.75). Thus, in this figure, for each integration point (IP) in the domain of interest, when $r_{apt} < 0.75$, red color is designated and when $r_{apt} \geq 0.75$, black color is attributed. It is clear that at the beginning of the ground motion, some instability points (black points)

are shown in the foundation layer. However, at 7 seconds, which is the end of the strong phase, additional instability points appear in the foundation and increase upwards towards the slope of the embankment (Figure 7b).

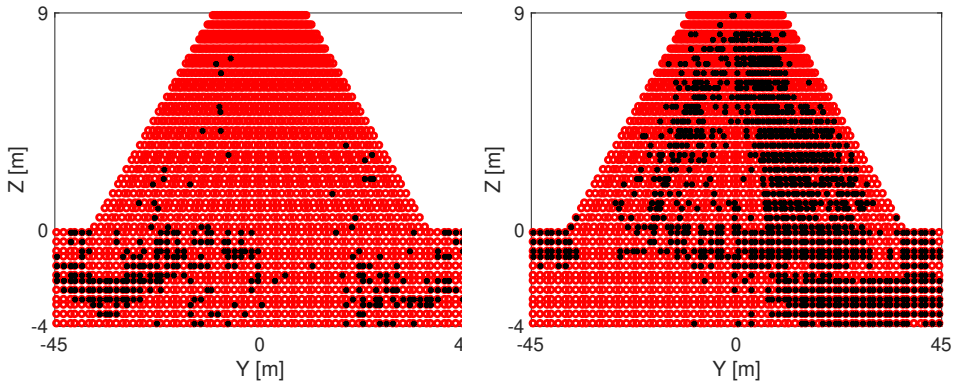

(a) t = 3s (b) t = 7s

Figure 7: The distribution of $r_{apt} \geq 0.75$ from the IPs (black points) for the example ground motion

In order to statistically represent the values of r_{apt} during the co-seismic duration of the example ground motion, Figure 8a shows the empirical Complementary Cumulative Distribution Function (CCDF) of this parameter. The limit value of 0.75 is also plotted as a dashed line in this figure. As expected, the CCDF of r_{apt} evolves with the increase in time. It may also be interpreted that the probability of exceeding the limit value of 0.75 increases with time. Because r_{apt} can be interpreted as a LFS, its global representation can be defined as the probability of exceeding the r_{apt} limit value, which is going to be introduced in this paper as the *failure density concept*. This later intends to give a measure of the failure extension in the embankment,

and is defined in Equation 13 such as:

$$\mathbb{P}(r_{apt}(t) \geq 0.75) = \int_{r_{apt} \geq 0.75} f(r_{apt}) \cdot dr_{apt} \approx \frac{N_{r_{apt} \geq 0.75}(t)}{N_T} = \rho_{r_{apt} \geq 0.75}(t) \quad (13)$$

$N_{r_{apt} \geq 0.75}(t)$ gives the number of IPs that surpassed the r_{apt} limit and N_T is the total number of IPs in the domain of interest (2484 in this case).

Therefore, having two global damage indices: $u_{z,rel}$ and $\rho_{r_{apt}}$, it will be interesting to compare them to understand the potential failure of the embankment. For this purpose, Figure 8b shows the variation in time of both $u_{z,rel}$ and $\rho_{r_{apt} \geq 0.75}$ and points out on the fact that they are linked. For example, around 5 seconds, the settlement increases when $\rho_{r_{apt} \geq 0.75}$ increases. Once the settlement reaches a maximum value, $\rho_{r_{apt} \geq 0.75}$ reaches a peak value of 0.4. This value means that 40% of the domain of interest had $r_{apt} \geq 0.75$. It is interesting to mention that around 10 seconds, even if $u_{z,rel}$ was constant, $\rho_{r_{apt} \geq 0.75}$ was decreasing. This can be interpreted as the dissipation of the excess pore water pressure at this time (Figure 5b) and a proof that the soil tries to densify. At the end of the strong phase of the motion, the soil tries to recover where its settlement and r_{apt} are constants. Thus, for practical purposes, $\rho_{r_{apt} \geq 0.75}$ at the end of the ground motion is able to represent the state of failure of the embankment.

It can be partially concluded in this section that the damage measure represented by the relative crest settlement $\delta u_{z,rel}/H$ is a global indicator of the potential failure of the embankment. In addition, the ratio of apparent to critical friction angle, designated as the parameter r_{apt}, provides a reliable measure of soil strength, which takes into account the loading history and can be used as a criterion for estimating the local state of soil during cyclic loads. More importantly, this section interpreted the link between the global

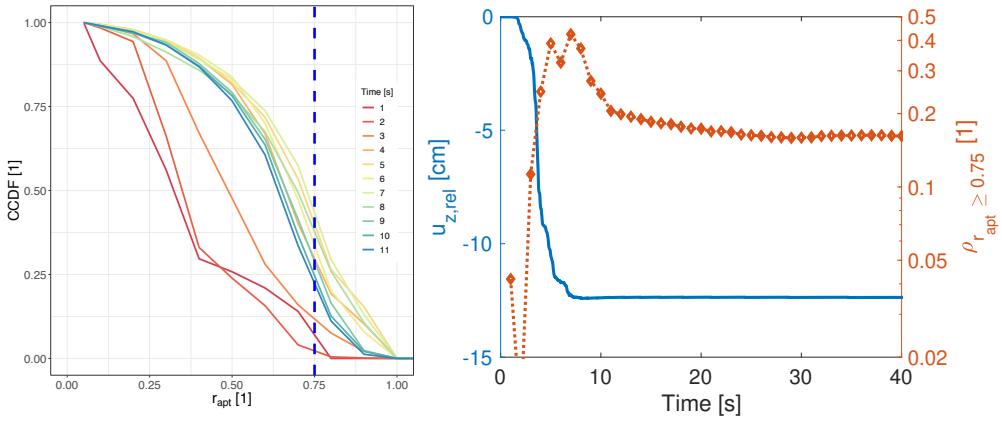

(a) (b)

Figure 8: a) The CCDF of the parameter r_{apt} during the co-seismic duration of the example ground motion and b) the dependency of the parameter r_{apt} with the crest settlement of the embankment

damage measure with the soil mechanical behavior via the predefined *failure density concept*.

Hence, it was presented in this paper a model to generate aftershocks and the analysis to interpret the potential embankment failure. In the coming section, one of the objectives of this paper will be developed, as to quantify the potential failure for sequences of mainshocks and aftershocks.

6. Damage measures during sequential clusters

The PBEE methodology provides a probabilistic description of the system-level performance of structures. It requires the calculation of an engineering demand parameter that can be related to the intensity measure of the occurred ground motions. Therefore, it was presented in Section 5, the potential structural failure and its link to the soil mechanical behavior. However, for

life cycle assessment, it is necessary to account for the build-up of seismic losses due to the damage issued from multiple events [11, 20, 19, among others].

In this study, 210 sequential cluster events of mainshocks-aftershocks are considered. It should be reminded that each sequence contains 44 acceleration time histories of mainshocks that were permuted 10 times. In order to be statistically representative of a large number of sequences, 21 subsets compatible with the seismic hazard of the site of concern were considered. In addition, as to take into account the recovery time of the embankment, 30 seconds are interposed between each mainshock and its corresponding first aftershock. The choice of this recovery duration was validated in the work of Khalil and Lopez-Caballero [26]. Since the used numerical model takes into consideration the damage history of the embankment, in this section, the evolution of the global response will be examined from the two damages indices that were presented in Section 5: $u_{z,rel}$ and $\rho_{r_{apt}}$. All over this paper, the notation *MS* designates *Mainshocks* and *AFS* designates *Aftershocks*.

6.1. Relative crest settlement for sequential earthquakes

The performance of the embankment during its lifetime is evaluated from its cumulative global damage measure. In the case of embankments (or dams), the damage is quantified from the percentage relative crest settlement $\delta u_{z,rel}/H$ where $u_{z,rel}$ is the crest settlement and H is the height of the embankment with the foundation (i.e. 19 m in this case) [60, 33, 26]. In order to classify the damage, levels are also attributed to the relative crest settlement. When $\delta u_{z,rel}/H \leq 0.02\%$, there is *No* damage, if $0.02\% < \delta u_{z,rel}/H \leq 0.1\%$, the damage is *Minor*, if $0.1\% < \delta u_{z,rel}/H \leq 1\%$, the

damage is *Moderate* and finally if $\delta u_{z,rel}/H > 1\%$, the damage is *Serious*. For the sake of brevity only, Figure 9 shows a comparison of $\delta u_{z,rel,cum}/H$ for two examples of MS and MS-AFS sequences in order to examine the effect of the aftershock occurrence. It should be mentioned that for each presented case in Figure 9, the permutation of the mainshock events is the same in both sequence types. The only difference is the aftershock occurrence.

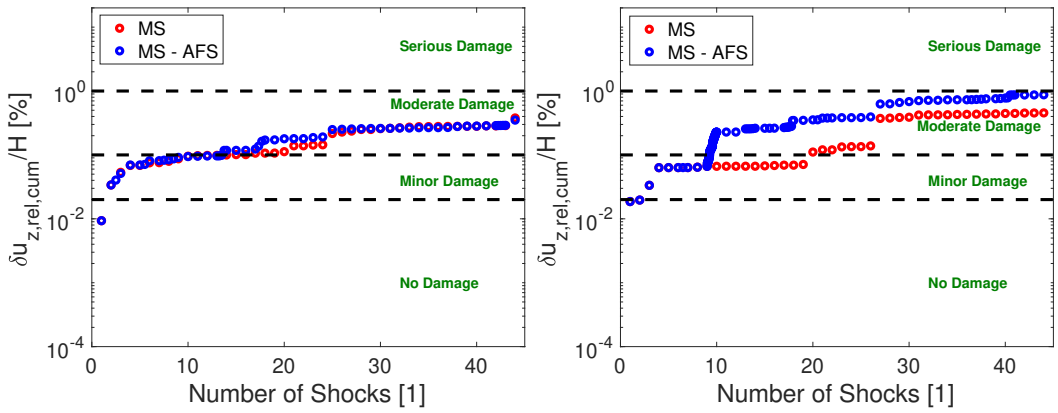

(a) Seq1 (b) Seq2

Figure 9: Comparison of the percentage relative crest settlement for examples of mainshock (MS) sequences and mainshocks - aftershocks (MS - AFS) sequences

Clearly, two typical behaviors can be identified. In Figure 9a, the global response during the lifetime of the embankment was almost similar for the two sequences. At a point in time, when the 17th shock occurred, a small peak in the damage appears for the MS-AFS sequences. It should be noted that this shock has 3 aftershocks. On the contrary, the damage for MS-AFS sequences in Figure 9b, has a rapid increase in the 9th shock so that it surpassed a damage level. It should be noted that this shock produced 70 aftershocks. After it, the damage was higher for the MS-AFS sequences,

until the end of the lifetime when the soil densifies and was subjected to multiple types of motions, the level of damage is the same. Thus, it should be remarked that the existence and the high number of aftershocks have a major importance on the lifetime behavior of the embankment due to the aging effect.

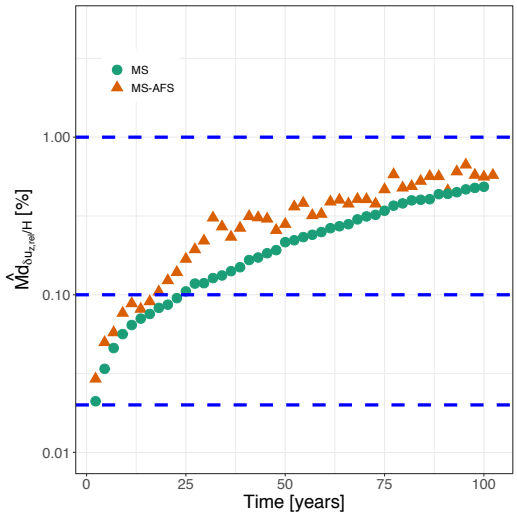

Figure 10: Median value of the crest settlement for the MS and MS-AFS sequences

In order to take into consideration all the tested sequences, the median estimator value of the cumulative relative crest settlement is shown in Figure 10. A comparison with the MS sequential type appears also in this figure. Clearly, the damage during the lifetime of the embankment is not the same, whereas at the beginning and the end of the lifetime, the cumulative crest settlement is slightly different between both sequences. However, for the level of damage, no remarkable difference is noted (i.e. at the end of the lifetime, *Moderate* damage was reached for MS and MS-AFS sequences).

It can be deduced from the comparison of the MS and MS-AFS sequences,

that the lifetime damage of the embankment could be affected by the occurrence and number of aftershocks. As for the level of damage, similarity between both sequences is identified. In order to understand the reason behind this behavior, a close examination of the damage index related to the soil residual strength is conducted in the next section.

6.2. Damage index from the soil residual strength

It was presented in Section 5 the parameter r_{apt} that provides, for any soil state, a direct measure of the "distance to reach the critical state". It varies from 0 and reaches perfect plasticity at 1. It could be defined as the inverse of a local safety factor ($r_{apt} = 1/LFS$). A threshold value of the damage measure is taken as 0.75 (i.e. corresponds to $LFS \approx 1.33$) [35, 43]. In addition, in the same cited section, the failure density concept represented by $\rho_{r_{apt} \geq 0.75}$ at the end of the ground motion, was presented. It was shown its ability to represent the state of failure of the embankment. In this section, similarly to Section 5, the link between the two global damage measures is shown in Figure 11 for an example of MS and for the same sequence with added aftershock occurrence. It should be mentioned that for the sake of clarity, the notation $\rho_{r_{apt} \geq 0.75}$ means $\rho_{r_{apt} \geq 0.75}(t = t_{end})$. The response of the embankment for this sequence example can be divided into three time intervals: before 30 years, between 30 and 60 years, and after 60 years. A discussion on each sequences will be developed and then a comparison of both types will proceed.

For the mainshock sequence in Figure 11a, before 30 years, $\rho_{r_{apt} \geq 0.75}$ slightly increases when $\delta u_{z,rel}/H$ was also increasing. The global damage for this duration is still acceptable. It should be remarked that for one shock

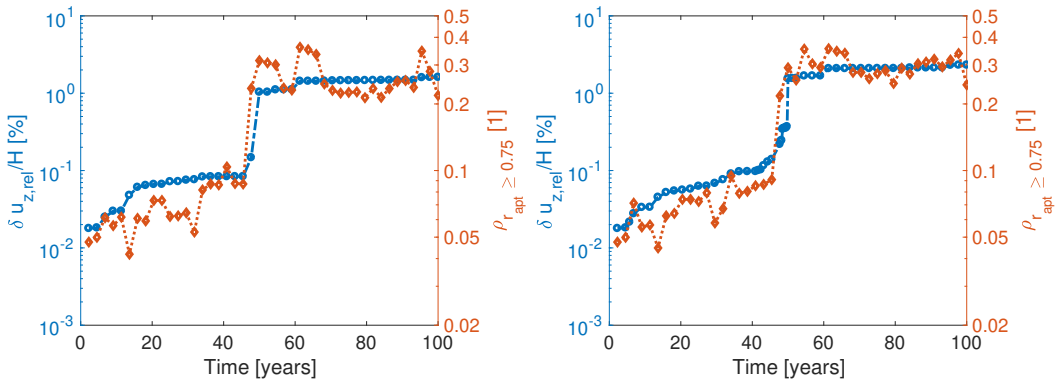

(a) MS (b) MS-AFS

Figure 11: The time evolution of $\delta u_{z,rel}/H$ and $\rho_{r_{apt}\geq 0.75}$ for a a) MS sequence and b) a MS-AFS sequence

at 18 years, the crest settlement increases whereas $\rho_{r_{apt}\geq 0.75}$ decreases, this means that this shock did not induce many local instabilities, or on the contrary it helped the soil to dissipate the residual excess pore water pressure Δp_w. Between 30 and 60 years, the behavior was almost similar to the previous time interval, however, at 50 years, $\delta u_{z,rel}/H$ increases rapidly to reach severe damages which induced instabilities in 30% of the domain of interest (i.e. $\rho_{r_{apt}\geq 0.75} = 0.3$). After 60 years, both damage measures are constants. For the aftershock occurrence in this example sequence (Figure 11b), no change in the response for two time intervals: before 20 yeas and after 60 years. However, between 30 and 60 years, the aftershocks prevented the rapid increase in the crest settlement and in $\rho_{r_{apt}\geq 0.75}$. It is interesting to mention that for both MS and MS-AFS sequences, at the end of the lifetime duration, the level of damage is the same. This result confirms the one deduced from the lifetime evolution of the relative crest settlement and also

verifies the link between both damage indices.

As to take into consideration more example sequences and the lifetime evolution of $\rho_{r_{apt}\geq 0.75}$, Figure 12 shows this parameter for two example sequences of MS and their corresponding sequences with aftershock occurrence. As expected, two typical behaviors can be identified: a similarity in the response during time, for example the sequence in Figure 12a, and a slight difference in the damage response specially after a strong shock (Figure 12b).

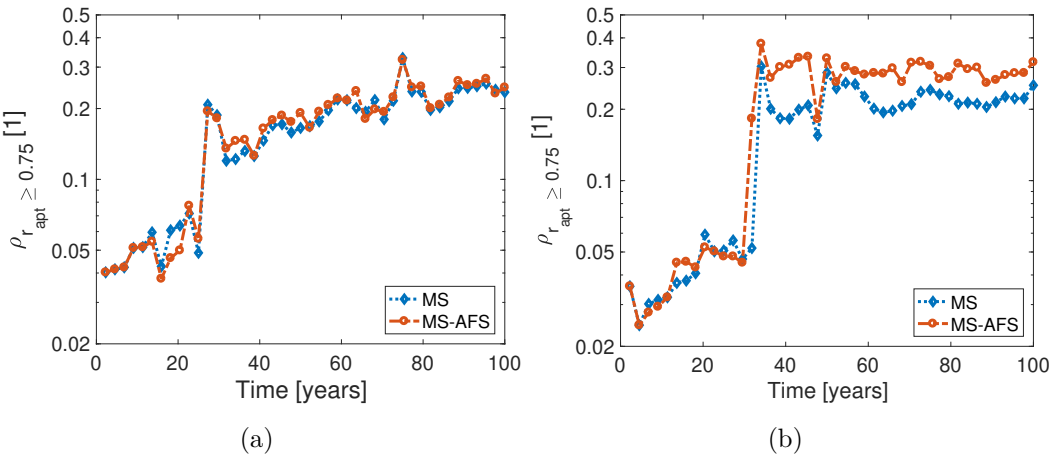

Figure 12: The time evolution of $\rho_{r_{apt}\geq 0.75}$ for two examples of MS or MS-AFS sequences

It can be partially concluded from this section, that the lifetime embankment failure, evaluated from two damage indices slightly differs between MS and MS-AFS sequences. The occurrence of AFS increases the damage during time, but, at the end of the working life, the damage of both sequences is slightly close and the level of damage is the same. The coming section will try to answer the second question of the Introduction section about the effect of the aftershocks occurrence on the lifetime distribution of the embankment.

7. Survival Functions of the tested sequences

Survival analysis is the time needed for an event of interest to occur. It is also called the time-to-event data [5, 24, 53, among others]. Survival analysis is represented by survival functions or hazard functions. They are both inversely proportional, so when the hazard increases the survival function decreases. This later estimates the lifetime distribution of a test model and more importantly its Mean Time To Failure (MTTF, the expected time to failure for a non-repairable system). Several approaches exist in order to calculate the survivors [15]. The approaches can be parametric and non-parametric. The commonly used method is the *Kaplan-Meier* estimator [23]. It is a non parametric method that does not need any assumption for the distribution of the survival time, or the relationship between the covariates and the survival time (please refer to Khalil and Lopez-Caballero [26] for more details).

Section 6 analyzed the damage measure of example sequences of MS and MS-AFS. In order to take into account all the tested sequences and evaluate their survival probability, a survival analysis is conducted to estimate the useful working life of the embankment. The survival functions for *Moderate* (DL3) and *Serious* (DL4) damage levels are shown in Figure 13. The MTTF and the *p-value* are indicated in this figure. Typically, if the *p-value* $\leq 5\%$, the null hypothesis H_0 is rejected, and vice versa. The null hypothesis H_0 in the case of this study is to state that there is no difference in the lifetime distribution of the embankment between a MS or a MS-AFS sequence. In addition, an informative risk table shows the number of sequences that did not reach the precised damage level in a specific period of time.

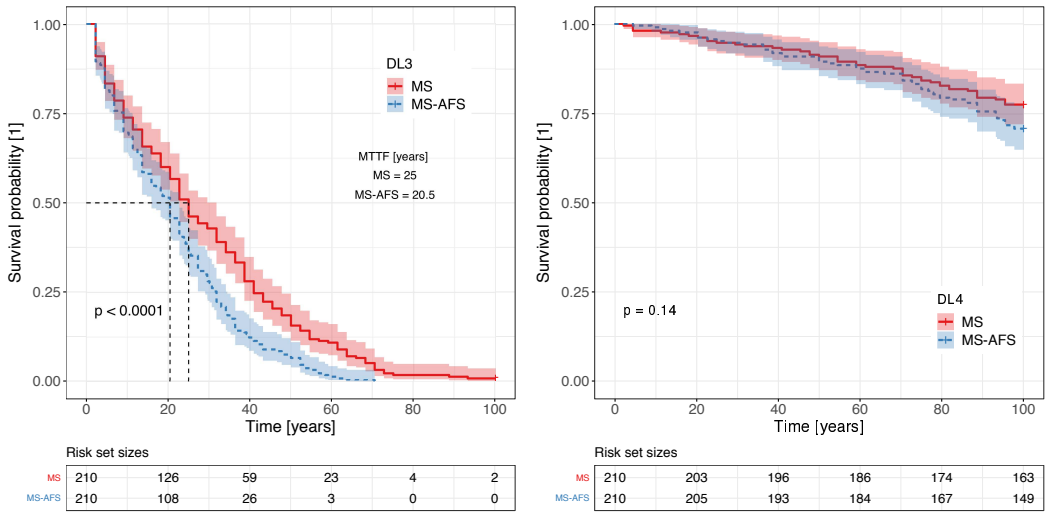

(a) DL3 (b) DL4

Figure 13: Survival functions of the two types of sequences used in this study for a) *Moderate* damage (DL3) and b) *Serious* damage (DL4)

Concerning the *Moderate* damage (or DL3, Figure 13a), the MTTF of both MS and MS-AFS sequences occurs within the useful life of the embankment (i.e. 100 years). However, the occurrence of aftershocks decreased the MTTF of the embankment for 5 years (i.e. 20.5 years instead of 25 years in the case of MS sequence). The risk table shows also that more sequences have reached *DL3* when the aftershocks occurred. For example, at 20 years, 126 MS sequences resisted this level of damage comparing to a decrease to 108 MS-AFS sequences that resisted it. Moreover, the *p-value* $\leq 5\%$, which means that H_0 is rejected and thus, there is a difference between the lifetime distribution of the MS and MS-AFS sequences for *Moderate* damage level. As for the *Serious* damage (or DL4, Figure 13b), the embankment maintains its initial performance and then starts to degrade. The survival

function did not reach its MTTF and the null hypothesis is accepted, thus, the two distributions are alike for this damage level. However, after 70 years, the lifetime distribution for *DL4* in the case of MS-AFS sequences is slightly different from that of the MS sequences. This remark can also be seen from the risk table. Thus, for *DL4*, the embankment might reach its MTTF for a time window greater than 100 years (e.g. 475 years). This means that for the same event rate of mainshocks, the number of shocks should be greater than 44 input motions in one sequence. Clearly, the survival probability is site and structure specific because it is controlled by the ground motions characteristics and the working life of the concerned structure.

It can be partially concluded that for the considered working life of the embankment, the aftershocks occurrence is important for small damage levels whereas it is not the case for high damage levels. This aspect was seen because the embankment for DL3, started to degrade directly after the first shock, however for DL4, it maintained its initial performance and then degraded with time.

Since the survival analysis can be interpreted as a probability of failure, the coming section will develop the classical way to calculate this probability (i.e. fragility curves) and evaluate it during the working time of the embankment.

8. Fragility Curves Evolution

From Section 7, it was found that for *Moderate* damage level, the lifetime distribution of the MS and MS-AFS sequences is not the same, on the opposite to *Serious* damage level. In this section, and because the fragility

curves are commonly used for seismic loss estimation and risk management, their time evolution will be assessed. Classical fragility curves represent the failure probability of one event of given intensity [56, 50, 71, 19, among others]. However, for life cycle assessment, it is necessary to account for the build-up of seismic losses because of the damage in multiple events. In addition, the fragility functions are developed from *independent and identically distributed* observations. Hence, it is difficult to conduct the fragility curves for the cluster earthquakes since the aftershocks depend on their corresponding mainshock. More importantly, the history of loading in the soil plays a major role in its future behavior, which emphasizes the importance of the sequential analysis [26]. In order to overcome these challenges, the evolution of the fragility curves during the lifetime of the embankment proposed in this study is summarized in Figure 14.

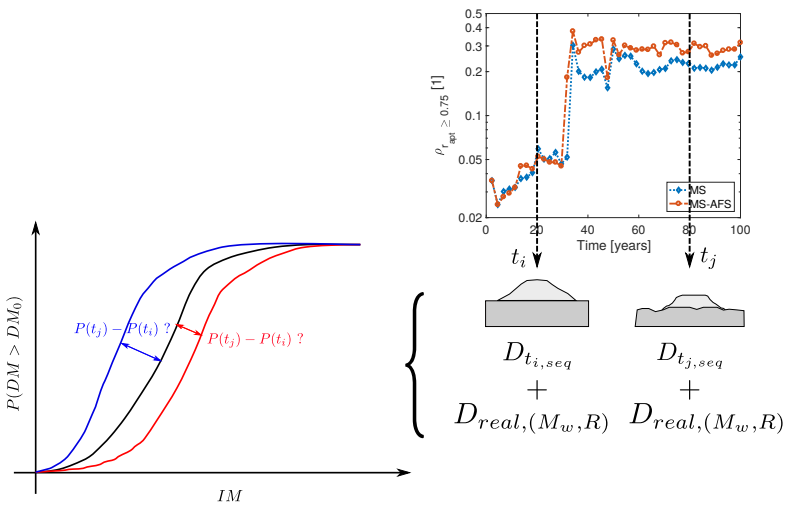

Figure 14: The methodology presented in this section

For different time intervals during a MS-AFS sequence, the damage state

of the embankment is not the same. For each corresponding state that is considered as a new initial state (site and structure specific), the damage is calculated after a number of unchained real motions (structure-specific) in order to calculate the fragility curves. Thus, the total induced damage is the one produced from the cumulative damage at $t = t_i$ resulted from the MS-AFS sequence added to the one produced from unchained ground motions (i.e. $D_{tot} = D_{cum_{ms-afs}(t_i)} + D_{real}$). According to that, and given the IM corresponding to the real ground motions, the evolution in time of the fragility curves is calculated. In the case of this work, the real ground motions are events ranged between 5.2 and 7.6 in magnitude and a site-to-source distances from 15 to 50 km. The MS-AFS sequence taken as an example is shown in Figure 15 and the years interval after which the fragility curves will be calculated are 0, 11, 22, 45 and 100 years (dashed lines).

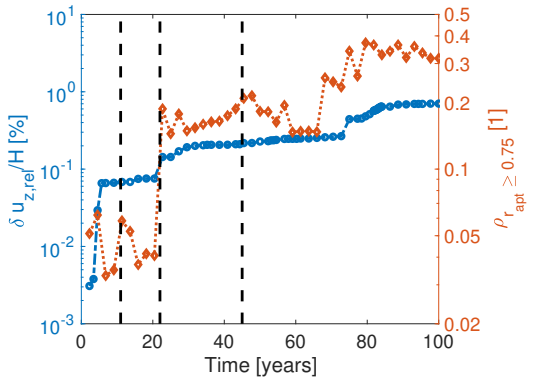

Figure 15: The MS-AFS sequence example and the time interval after which the fragility curves will be calculated

First, in order to examine the evolution of the global response of the embankment after each time interval, its damage measure is drawn in Figure 16a. It should be noted that in this figure, "NH" means "no history" and

"WH" means "with history". Taking as a reference the damage at $t_0 = 0$, which means when the embankment did not have a loading history, the evolution of $\delta u_{z,rel}/H$ shows that the crest settlement increases when the time increases. It is interesting to mention that for longer t_0, the history of loading delays the arrival to high values of $\delta u_{z,rel}/H$ that are compatible with the referenced values (at $t_0 = 0$).

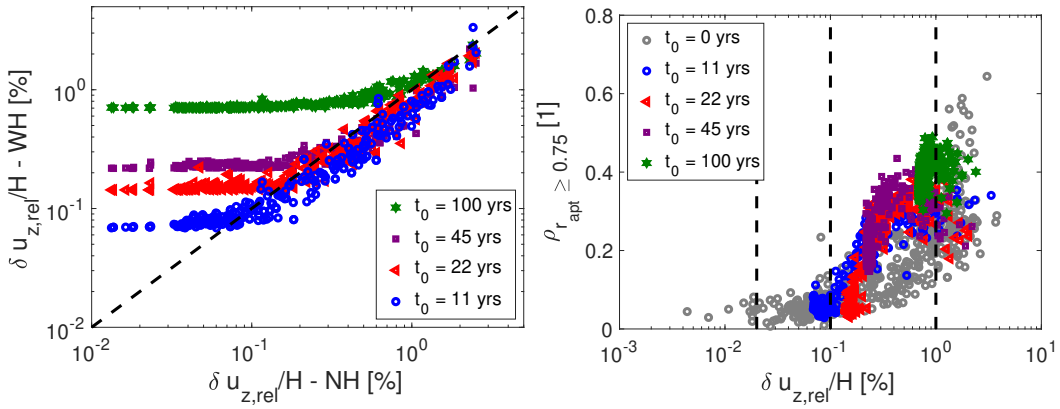

(a) (b)

Figure 16: The time evolution of the crest settlement $\delta u_{z,rel}/H$ and the density parameter $\rho_{r_{apt}}$

Concerning the second damage index related to the soil's residual strength, $\rho_{r_{apt}\geq 0.75}$, and its link with $\delta u_{z,rel}/H$, Figure 16b shows that for a short life-time duration (i.e. $t_0 = 11$ or 22 years), $\delta u_{z,rel}/H$ and $\rho_{r_{apt}\geq 0.75}$ were still acceptable. In addition, the results overlap with the ones of $t_0 = 0$. This indicates that sometimes, the short term analysis may be enough to represent the performance of the embankment. However, for higher values of t_0, both $\delta u_{z,rel}/H$ and the density parameter $\rho_{r_{apt}\geq 0.75}$ showed important values with a tendency to regain the initial values at $t_0 = 0$. This result emphasizes the

need to consider sequential analysis to understand the global performance of the structure during its lifetime.

As for the calculation of the fragility curves, two-parameter log-normal distribution functions are used (Equation 14) and are estimated from the maximum likelihood method [56, 50]. In addition, the quality of fit and the estimation of the confidence intervals are conducted from the methodology presented in the work of Sáez et al. [50]. Considering a threshold damage measure DM_0, an IM of level im and the "initial" damage $D_{t_0,seq}$ issued from the MS-AFS sequence, the fragility curve has the following form:

$$P(DM > DM_0|IM = im_{(M_w,R)}, D_{t_0,seq}) \quad = \quad \phi\left[\frac{\ln im - \ln \eta_{DM|IM}}{\beta_{DM|IM}}\right] \qquad (14)$$

where $\phi[.]$ is the standardized normal distribution function. $\eta_{DM|IM}$ is the median threshold value of IM required to cause the damage and $\beta_{DM|IM}$ is the total lognormal standard deviation. One or more IMs can be used to represent the fragility curves [33]. In this study, the intensity measure is the outcrop acceleration $a_{max,out}$, and the damage levels are *Moderate* and *Serious*. The results are shown in Figure 17. The solid line in this figure shows the response of the embankment without a past history which means at $t_0 = 0$.

Clearly, from Figure 17, the fragility curves evolves with time. At 11 years, the probability of exceeding the *Moderate* damage level depends on the severity of the ground motion that happened during this time (Figure 17a). For example, for ground motions of accelerations less than 0.2 g, the fragility curve is lower than that at $t_0 = 0$. However, greater than 0.2 g and for this short time interval, the embankment reaches failure faster when it has a history of loading. It should be mentioned that the other time intervals

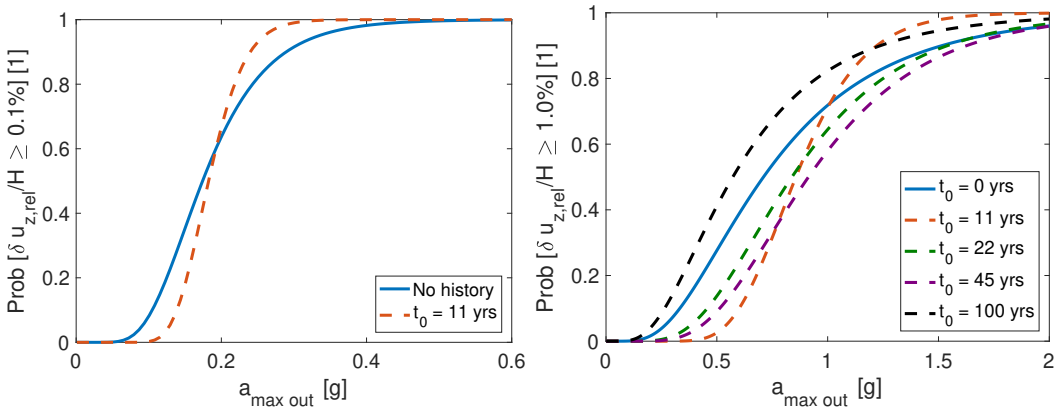

(a) (b)

Figure 17: The evolution in time of the probability of exceeding the a) *Moderate* and b) the *Serious* damage level

(i.e. 22, 45 and 100 years) are not drawn for this damage level, since their probability of failure is 1. As seen in Figure 15, the new "initial" state of the embankment after those time intervals has already surpassed the *Moderate* damage level. Concerning the *Serious* damage level in Figure 17b, also for t_0 = 11 years, the probability of failure depended on the severity of the ground motion. However, at 22 and 45 years, the fragility curves is lower than that at $t_0 = 0$. Thus, it can be deduced that the embankment resisted the applied load better than the beginning of its lifetime. This results points out the importance of the soil history of loading that affects its future behavior and may result in soil densification. Nevertheless, at 100 years, the probability of failure increases, and the embankment resistance to the amount of loading decreases.

In order to take into account different sequence example, Figure 18 shows the fragility curve of the *Serious* damage evolution for two other example se-

quences having different permutations of their mainshock occurrence. First, it can be seen that the result of this case is different from that in Figure 17b. For the same IM, in the case of sq14, the probability of failure decreases at the beginning of the lifetime, indicating a soil densification, after that an increase starts at 43 years. However, for higher time intervals, the probability of exceeding this damage level increases. It is interesting to notice that sq14 and sq48, at almost close t_0 (i.e. purple and yellow curves), showed completely opposite behavior. sq14 indicates a probability of failure close to that at $t_0 = 0$, however, sq48 shows an increase in this probability.

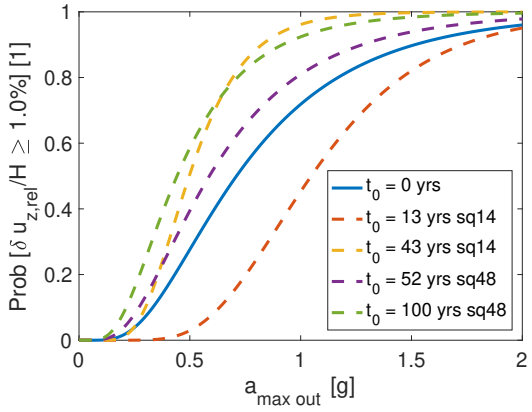

Figure 18: The evolution in time of the probability of exceeding the *Serious* damage level for different sequence examples

Thus, it can be deduced from these results, that the initial state of the embankment for each selected time interval is site-specific and is affected by the history of loading. Otherwise, the fragility curve computation is somehow a structure-specific approach. The probability of collapse decreases if the embankment tends to densify due to its history of loading, or the opposite if its initial state was already excessively damaged. It should be reminded

that the embankment during its lifetime was not subjected to any type of reinforcement or amelioration.

9. Discussions and Conclusions

In the present paper, the work focuses on the effect of the aftershock occurrence on the liquefaction-induced settlement on the embankment. It presented a model to generate the aftershocks which is based on the probabilistic version of the BASS model and is inspired by Turcotte et al. [63] and Hu et al. [16]. Moreover, this work developed a methodology to take into account the fragility curve evolution during the lifetime of the studied embankment that analyses its potential failure and the link with the soil mechanical behavior. For the sake of simplicity, the same database was used to generate both MS and AFS ground motions (i.e. the stochastic ground motion model proposed by Rezaeian and Der Kiureghian [44]).

It is important to mention that any other approaches could be implemented, if needed, under the proposed methodology of this paper. Since the proposed model is highly flexible, some aspects can be refined or modified if there is a need to capture specific characteristics of the seismic environment. In addition, the embankment was build on a layered homogeneous model. However, in practice, significant material heterogeneities may exist.

As a conclusion of this work, the presented findings are based on the results corresponding to the soil behavior model and the stochastic ground motion model adopted in this work. Thus, the answers to the questions presented in the introduction are cited correspondingly:

a) During sequential earthquakes, the cumulative damage of the embank-

ment is affected by the sequence type. It was shown in this paper that the damage is higher for sequences with aftershocks (i.e. MS-AFS) than the ones without the aftershocks occurrence (i.e. MS).

b) The survival functions with their MTTFs values, showed that the consideration of the aftershocks events is important for moderate levels of damage. However, the embankment survived high damage levels for a working life of 100 years.

c) The evolution of the fragility curves depends on the sequence type, and more importantly the initial soil state. It should be mentioned that the fragility functions were not computed for the sequential cluster events themselves due to some challenges (i.e. dependency of the mainshock and aftershock events, the randomness of the aftershock occurrence and the soil history of loading). Instead, it was evolved for some time intervals of a sequence example, after a bundle of unchained recorded ground motions. It was shown that the probability of failure is unpredictable because it either increases or decreases from the very initial probability of failure at $t_0 = 0$.

Acknowledgement

This work, within the ISOLATE project, benefited from French state funding managed by the National Research Agency reference under program Mobility and Sustainable Urban Systems (DS06) 2017 reference No. ANR-17-CE22-0009. The research reported in this paper has been supported in part by the SEISM Paris Saclay Research Institute.

References

[1] Li, C., Ji, D., Zhai, C., Ma, Y. and Xie, L. (2023). Vertical ground motion model for the nga-west2 database using deep learning method. *Soil Dynamics and Earthquake Engineering*, 165:107713.

[2] Aristizábal, C., Bard, P.-Y., Beauval, C., and Gómez, J. (2018). Integration of site effects into probabilistic seismic hazard assessment (PSHA): A comparison between two fully probabilistic methods on the euroseistest site. *Geosciences*, 8(8):285.

[3] Aubry, D., Chouvet, D., Modaressi, A., and Modaressi, H. (1986). Gefdyn: Logiciel d'analyse de comportement mécanique des sols par éléments finis avec prise en compte du couplage sol-eau-air. *Manuel scientifique, Ecole Centrale Paris, LMSS-Mat.*

[4] Aubry, D., Hujeux, J., Lassoudiere, F., and Meimon, Y. (1982). A double memory model with multiple mechanisms for cyclic soil behaviour. In *Proceedings of the Int. Symp. Num. Mod. Geomech*, pages 3–13.

[5] Bradburn, M. J., Clark, T. G., Love, S., and Altman, D. (2003). Survival analysis part ii: multivariate data analysis–an introduction to concepts and methods. *British journal of cancer*, 89(3):431–436.

[6] Causse, M., Laurendeau, A., Perrault, M., Douglas, J., Bonilla, L. F., and Guéguen, P. (2014). Eurocode 8-compatible synthetic time-series as input to dynamic analysis. *Bulletin of Earthquake Engineering*, 12(2):755–768.

[7] Christodoulou, S. E. and Fragiadakis, M. (2014). Vulnerability assessment of water distribution networks considering performance data. *Journal of Infrastructure Systems*, 21(2):04014040.

[8] Cosenza, E. and Manfredi, G. (2000). Damage indices and damage measures. *Progress in Structural Engineering and Materials*, 2(1):50–59.

[9] Di Sarno, L. and Pugliese, F. (2020). Seismic fragility of existing RC buildings with corroded bars under earthquake sequences. *Soil Dynamics and Earthquake Engineering*, 134:106169.

[10] Diamoutene, A., Barro, D., Somda, S. M. A., Noureddine, F., and Kamsu-Foguem, B. (2016). Survival analysis in living and engineering sciences. *JP Journal of Biostatistics*, 13(2):223–238.

[11] Ghosh, J., Padgett, J. E., and Sánchez-Silva, M. (2015). Seismic damage accumulation in highway bridges in earthquake-prone regions. *Earthquake Spectra*, 31(1):115–135.

[12] Goda, K. (2012). Nonlinear response potential of mainshock–aftershock sequences from japanese earthquakes. *Bulletin of the Seismological Society of America*, 102(5):2139–2156.

[13] Hatzigeorgiou, G. D. and Beskos, D. E. (2009). Inelastic displacement ratios for SDOF structures subjected to repeated earthquakes. *Engineering Structures*, 31(11):2744 – 2755.

[14] Holliday, J. R., Turcotte, D. L., and Rundle, J. B. (2008). Self-similar branching of aftershock sequences. *Physica A: Statistical Mechanics and its Applications*, 387(4):933–943.

765 [15] Hosmer Jr, D. W. and Lemeshow, S. (1999). Applied survival analysis:
766 regression modelling of time to event data. *Eur Orthodontic Soc*, pages
767 561–2.

768 [16] Hu, S., Gardoni, P., and Xu, L. (2018). Stochastic procedure for the
769 simulation of synthetic main shock-aftershock ground motion sequences.
770 *Earthquake Engineering & Structural Dynamics*, 47(11):2275–2296.

771 [17] Huang, S. L. and Yamasaki, K. (1993). Slope failure analysis using local
772 minimum factor-of-safety approach. *Journal of Geotechnical Engineering*,
773 119(12):1974–1989.

774 [18] Hujeux, J. (1985). Une loi de comportement pour le chargement cyclique
775 des sols. *Génie parasismique*, pages 287–302.

776 [19] Iervolino, I., Chioccarelli, E., and Suzuki, A. (2020). Seismic damage
777 accumulation in multiple mainshock-aftershock sequences. *Earthquake En-*
778 *gineering & Structural Dynamics*, 49(10):1007–1027.

779 [20] Iervolino, I., Giorgio, M., and Polidoro, B. (2015). Reliability of
780 structures to earthquake clusters. *Bulletin of Earthquake Engineering*,
781 13(4):983–1002.

782 [21] Ji, D., Wen, W., and Zhai, C. (2021). Constant-ductility energy factors
783 of sdof systems subjected to mainshock–aftershock sequences. *Earthquake*
784 *Spectra*, 37(2):1078–1107.

785 [22] Ji, J., Zhang, W., Zhang, T., and Song, J. (2023). Seismic displacement
786 of earth slopes incorporating co-seismic accumulation of dynamic pore wa-

ter pressure. *Earthquake Engineering & Structural Dynamics*, 52(6):1884–1907.

[23] Kaplan, E. L. and Meier, P. (1958). Nonparametric estimation from incomplete observations. *Journal of the American Statistical Association*, 53(282):457–481.

[24] Kartsonaki, C. (2016). Survival analysis. *Diagnostic Histopathology*, 22(7):263 – 270. Mini-Symposium: Medical Statistics.

[25] Kawase, H. (2011). Strong motion characteristics and their damage impact to structures during the off pacific coast of tohoku earthquake of march 11, 2011: How extraordinary was this M9.0 earthquake. In *4th IASPEI/IAEE International Symposium:Effects of Surface Geology on Seismic Motion*. University of California Santa Barbara.

[26] Khalil, C. and Lopez-Caballero, F. (2021). Survival analysis of a liquefiable embankment subjected to sequential earthquakes. *Soil Dynamics and Earthquake Engineering*, 140:106436.

[27] Kourkoulis, R., Anastasopoulos, I., Gelagoti, F., and Gazetas, G. (2010). Interaction of foundation- structure systems with seismically precarious slopes: Numerical analysis with strain softening constitutive model. *Soil Dynamics and Earthquake Engineering*, 30(12):1430–1445.

[28] Kramer, S. L. (1996). *Geotechnical earthquake engineering*. Pearson Education.

[29] Kuhl, D. and Crisfield, M. A. (1999). Energy-conserving and decaying

algorithms in non-linear structural dynamics. *International Journal for Numerical Methods in Engineering*, 45(5):569–599.

[30] Li, Q. and Ellingwood, B. R. (2007). Performance evaluation and damage assessment of steel frame buildings under main shock-aftershock earthquake sequences. *Earthquake Engineering & Structural Dynamics*, 36(3):405–427.

[31] Li, Y., Song, R., and Lindt, J. W. V. D. (2014). Collapse fragility of steel structures subjected to earthquake mainshock-aftershock sequences. *Journal of Structural Engineering*, 140(12):04014095.

[32] Lopez-Caballero, F., Aristizábal, C., and Sánchez-Silva, M. (2020). A model to estimate the lifetime of structures located in seismically active regions. *Engineering Structures*, 215:110662.

[33] Lopez-Caballero, F. and Khalil, C. (2018). Vulnerability assessment for earthquake liquefaction–induced settlements of an embankment using gaussian processes. *ASCE-ASME Journal of Risk and Uncertainty in Engineering Systems, Part A: Civil Engineering*, 4(2):04018010.

[34] Lopez-Caballero, F. and Modaressi-Farahmand-Razavi, A. (2010). Assessment of variability and uncertainties effects on the seismic response of a liquefiable soil profile. *Soil Dynamics and Earthquake Engineering*, 30(7):600–613.

[35] Lopez-Caballero, F. and Modaressi-Farahmand-Razavi, A. (2013). Numerical simulation of mitigation of liquefaction seismic risk by preloading

and its effects on the performance of structures. *Soil Dynamics and Earthquake Engineering*, 49:27 – 38.

[36] Lopez-Caballero, F., Modaressi-Farahmand-Razavi, A., and Stamatopoulos, C. A. (2016). Numerical evaluation of earthquake settlements of road embankments and mitigation by preloading. *International Journal of Geomechanics*, 16(5):C4015006.

[37] Lu, N., Sener-Kaya, B., Wayllace, A., and Godt, J. W. (2012). Analysis of rainfall-induced slope instability using a field of local factor of safety. *Water Resources Research*, 48(9).

[38] Modaressi, H. and Benzenati, I. (1994). Paraxial approximation for poroelastic media. *Soil Dynamics and Earthquake Engineering*, 13(2):117 – 129.

[39] Nafday, A. M. (2010). Soil liquefaction modelling by survival analysis regression. *Georisk*, 4(2):77–92.

[40] Pan, H. and Kusunoki, K. (2020). Aftershock damage prediction of reinforced-concrete buildings using capacity spectrum assessments. *Soil Dynamics and Earthquake Engineering*, 129:105952.

[41] Panchireddi, B. and Ghosh, J. (2019). Cumulative vulnerability assessment of highway bridges considering corrosion deterioration and repeated earthquake events. *Bulletin of earthquake engineering*, 17(3):1603–1638.

[42] Rapti, I. (2016). *Numerical modeling of liquefaction-induced failure of geostructures subjected to earthquakes*. Theses, Université Paris-Saclay - CentraleSupélec.

[43] Rapti, I., Lopez-Caballero, F., Modaressi-Farahmand-Razavi, A., Foucault, A., and Voldoire, F. (2018). Liquefaction analysis and damage evaluation of embankment-type structures. *Acta Geotechnica*, 13(5):1041–1059.

[44] Rezaeian, S. and Der Kiureghian, A. (2012). Simulation of orthogonal horizontal ground motion components for specified earthquake and site characteristics. *Earthquake Engineering & Structural Dynamics*, 41(2):335–353.

[45] Riascos-Ochoa, J., Sánchez-Silva, M., and Klutke, G.-A. (2016). Modeling and reliability analysis of systems subject to multiple sources of degradation based on lévy processes. *Probabilistic Engineering Mechanics*, 45:164–176.

[46] Ruiz-García, J. (2012). Mainshock-aftershock ground motion features and their influence in building's seismic response. *Journal of Earthquake Engineering*, 16(5):719–737.

[47] Ruiz-García, J. (2014). Discussion on "effects of multiple earthquakes on inelastic structural response". *Engineering Structures*, 58:110–111.

[48] Ruiz-Garcia, J. and Negrete-Manriquez, J. C. (2011). Evaluation of drift demands in existing steel frames under as-recorded far-field and near-fault mainshock-aftershock seismic sequences. *Engineering Structures*, 33(2):621 – 634.

[49] Sadeghi, H., Kimoto, S., Oka, F., and Shahbodagh, B. (2014). Dynamic analysis of river embankments during earthquakes using a finite deformation FE analysis method. In *14th International Conference of the Interna-*

877 *tional Association for Computer Methods and Advances in Geomechanics*,
878 number 2011, pages 637–642.

879 [50] Sáez, E., Lopez-Caballero, F., and Modaressi-Farahmand-Razavi, A.
880 (2011). Effect of the inelastic dynamic soil-structure interaction on the
881 seismic vulnerability assessment. *Structural Safety*, 33(1):51 – 63.

882 [51] Salami, M. R., Kashani, M. M., and Goda, K. (2019). Influence of
883 advanced structural modeling technique, mainshock-aftershock sequences,
884 and ground-motion types on seismic fragility of low-rise RC structures.
885 *Soil Dynamics and Earthquake Engineering*, 117:263 – 279.

886 [52] Sanchez-Silva, M., Klutke, G.-A., and Rosowsky, D. V. (2011). Life-cycle
887 performance of structures subject to multiple deterioration mechanisms.
888 *Structural Safety*, 33(3):206 – 217.

889 [53] Schober, P. and Vetter, T. R. (2018). Survival analysis and interpre-
890 tation of time-to-event data: The tortoise and the hare. *Anesthesia and*
891 *analgesia*, 127(3):792.

892 [54] Serrano, J. A., Bojórquez, E., Bojórquez, J., Reyes-Salazar, A., Torres,
893 I., Ruiz-García, J., Formisano, A., Fernández, E., Leyva, H., and Llanes-
894 Tizoc, M. D. (2023). Ratio of hysteretic and input energy spectra for
895 nonlinear structures under seismic sequences. *Sustainability*, 15(6).

896 [55] Shcherbakov, R., Turcotte, D. L., and Rundle, J. B. (2005). Aftershock
897 statistics. *Pure and Applied Geophysics*, 162(6-7):1051–1076.

[56] Shinozuka, M., Feng, M. Q., Lee, J., and Naganuma, T. (2000). Statistical analysis of fragility curves. *Journal of Engineering Mechanics*, 126(12):1224–1231.

[57] Shokrabadi, M. and Burton, H. V. (2018). Risk-based assessment of aftershock and mainshock-aftershock seismic performance of reinforced concrete frames. *Structural Safety*, 73:64 – 74.

[58] Shome, N. (1999). *Probabilistic Seismic Demand Analysis of Nonlinear Structures*. Stanford University.

[59] Sica, S., Pagano, L., and Modaressi, A. (2008). Influence of past loading history on the seismic response of earth dams. *Computers and Geotechnics*, 35(1):61 – 85.

[60] Swaisgood, J. (2003). Embankment dam deformations caused by earthquakes. In *PCEE 2003: 7th Pacific Conference on Earthquake Engineering, University of Canterbury, Christchurch, New Zealand, Conference Handbook*, page Paper 014. New Zealand Society for Earthquake Engineering.

[61] Trevlopoulos, K., Guéguen, P., Helmstetter, A., and Cotton, F. (2020). Earthquake risk in reinforced concrete buildings during aftershock sequences based on period elongation and operational earthquake forecasting. *Structural Safety*, 84:101922.

[62] Tsaparli, V., Kontoe, S., Taborda, D. M. G., and Potts, D. M. (2016). Vertical ground motion and its effects on liquefaction resistance of fully

saturated sand deposits. *Proceedings of the Royal Society A: Mathematical, Physical and Engineering Sciences*, 472(2192):20160434.

[63] Turcotte, D. L., Holliday, J. R., and Rundle, J. B. (2007). BASS, an alternative to ETAS. *Geophysical Research Letters*, 34(12):L12303.

[64] Utsu, T. (1970). Aftershocks and earthquake statistics (1): Some parameters which characterize an aftershock sequence and their interrelations. *Journal of the Faculty of Science, Hokkaido University. Series 7, Geophysics*, 3(3):129–195.

[65] Vamvatsikos, D. and Cornell, C. A. (2002). Incremental dynamic analysis. *Earthquake Engineering & Structural Dynamics*, 31(3):491–514.

[66] Wen, W., Ji, D., and Zhai, C. (2020). Cumulative damage of structures under the mainshock-aftershock sequences in the near-fault region. *Journal of Earthquake Engineering*, pages 1–15.

[67] Wen, W., Zhai, C., Ji, D., Li, S., and Xie, L. (2017). Framework for the vulnerability assessment of structure under mainshock-aftershock sequences. *Soil Dynamics and Earthquake Engineering*, 101:41–52.

[68] Yang, J. (2004). Reappraisal of vertical motion effects on soil liquefaction. *Géotechnique*, 54(10):671–676.

[69] Yeo, G. L. and Cornell, C. A. (2009). Building life-cycle cost analysis due to mainshock and aftershock occurrences. *Structural Safety*, 31(5):396–408.

[70] Yoder, M. R., Van Aalsburg, J., Turcotte, D. L., Abaimov, S. G., and Rundle, J. B. (2013). Statistical variability and tokunaga branching of

aftershock sequences utilizing bass model simulations. *Pure and Applied Geophysics*, 170(1):155–171.

[71] Zentner, I. (2017). A general framework for the estimation of analytical fragility functions based on multivariate probability distributions. *Structural Safety*, 64:54 – 61.

[72] Zhai, C.-H., Wen, W.-P., Chen, Z., Li, S., and Xie, L.-L. (2013). Damage spectra for the mainshock–aftershock sequence-type ground motions. *Soil Dynamics and Earthquake Engineering*, 45:1–12.

[73] Zhang, L., Goda, K., De Luca, F., and De Risi, R. (2020). Mainshock-aftershock state-dependent fragility curves: A case of wood-frame houses in british columbia, canada. *Earthquake Engineering & Structural Dynamics*, 49(9):884–903.

[74] Zienkiewicz, C. (1991). The finite element method; solid and fluid mechanics. *Dynamics and Non-Linearity*, 2:219.